



Cite this: *Energy Adv.*, 2022,
1, 99

Production of jet fuel-range hydrocarbon biofuel by hydroxyalkylation–alkylation of furfural with 2-methylfuran and hydrodeoxygenation of C₁₅ fuel precursor over a Ni/ γ -Al₂O₃ catalyst: a reaction mechanism†

Alekhya Kunamalla,  Bhushan S. Shrirame and Sunil K. Maity *

This study presents manufacturing jet fuel-range (C₉–C₁₅) hydrocarbon biofuels from 2-methylfuran and furfural. The process involves a hydroxyalkylation–alkylation reaction, followed by hydrodeoxygenation of the C₁₅ fuel precursor. The hydroxyalkylation–alkylation reaction was investigated under various cation exchange resin loadings, furfural/2-methylfuran molar ratios, and reaction temperatures. The hydroxyalkylation–alkylation reaction results were further corroborated by an appropriate kinetic model. Hydrodeoxygenation proceeds via the sequential furan ring-hydrogenation and ring-opening reactions, followed by the combination of dehydroformylation, hydrodeoxygenation, and cracking reactions. The dehydroformylation reaction was the leading pathway over a Ni/ γ -Al₂O₃ catalyst, forming mainly C₁₄H₃₀ alkane. The oxygenate conversion was boosted with rising hydrogen pressure, Ni metal content on γ -Al₂O₃, and reaction temperatures. Both hydrodeoxygenation and hydrogenation reactions proliferated at elevated hydrogen pressure with the enrichment of the C₁₅ alkane and ring-opening and ring-hydrogenation products. The cracking, ring-opening, and ring-hydrogenation reactions were promoted at elevated reaction temperatures with a significant amount of lighter alkanes.

Received 16th December 2021,
Accepted 15th January 2022

DOI: 10.1039/d1ya00078k

rsc.li/energy-advances

1. Introduction

At the moment, greater than 80% of the world's energy is derived from non-renewable coal, natural gas, and petroleum. With the rapid growth of the population and gradual expansion of economics, the energy demand in the world is continuously mounting and anticipated to increase by about 25% by 2040.¹ At present, diesel, jet fuel, and gasoline are the major transportation fuels, which account for nearly 28% of the primary energy consumption in the world.¹ Currently, jet fuel and diesel account for around 7% and 35% of the energy consumption in the transportation sector, and their demands are projected to rise by 55% and 45% in the coming 20 years, respectively.¹ Currently, transportation fuels are mainly produced by petroleum refining. Petroleum is, however, limited and depleting

rapidly. Moreover, the use of petroleum poses environmental issues owing to the release of poisonous and greenhouse gases. The quest for renewable automobile fuels is thus growing throughout the globe. Petroleum originates from the gradual decay of biomass for millions of years under intense heat and pressure. At present, biomass is the sole renewable source of carbon in our biosphere. Therefore, biomass is considered the potential substitute for petroleum to produce renewable transportation fuels, called biofuels. Similar to a petroleum refinery, the biomass is refined in a biorefinery to obtain various biofuels and value-added chemicals.

The lignocellulose biomass is the most abundant on the earth. It includes agriculture wastes, residues from forest management exercises, and various cellulosic energy crops. Significant progress has been made in the past to convert this biomass to biofuels, such as biobutanol, bioethanol, *etc.*² However, these are oxygen-containing biofuels with reduced fuel mileage and incongruity with refinery infrastructures. Continuous efforts are thus made for manufacturing biofuels comparable to present transportation fuels, called hydrocarbon biofuels.³ Fast pyrolysis,⁴ hydrothermal liquefaction,^{5,6} and biomass-to-liquid⁷ are some of the possible technologies for manufacturing hydrocarbon biofuels from lignocellulose

Department of Chemical Engineering, Indian Institute of Technology Hyderabad, Kandi, Sangareddy-502284, Telangana, India. E-mail: sunil_maity@che.iith.ac.in; Tel: +91-40-2301-6202

† Electronic supplementary information (ESI) available: GC-FID chromatograms for HAA reaction and gas-phase sample for HDO, GC-TCD chromatogram for HDO, kinetic and Arrhenius plots for HAA reaction, GC-FID chromatogram for HDO, HR-TEM images, and TPR and NH₃-TPD of the regenerated catalyst. See DOI: 10.1039/d1ya00078k



biomass. Alternatively, the carbohydrate fraction of the lignocellulose biomass can be converted to hydrocarbon biofuels *via* various intermediate and platform chemicals.⁸ Furfural finds a special place among the platform chemicals owing to its exceptional derivative potentials, including value-added chemicals, hydrocarbon biofuels, and fuel additives.⁹ Furfural is produced from the low-value hemicellulose fraction of lignocellulose biomass by a dehydrocyclization reaction using an acid catalyst. Furfural is a highly reactive oxygen-containing compound with poor fuel properties. The deoxygenation of furfural, however, produces C₄–C₅ hydrocarbons, which are inappropriate as transportation fuels. Therefore, the carbon–carbon coupling reaction, such as hydroxyalkylation–alkylation (HAA), is necessary to obtain transportation fuel precursors with a longer carbon chain length (Reaction 1). In the present study, the HAA reaction of furfural with 2-methylfuran (2-MF) was explored to produce the C₁₅ fuel precursor. 2-MF is generally derived from furfural by a selective hydrogenation reaction.¹⁰ Subsequent hydrodeoxygenation (HDO) of this C₁₅ fuel precursor produces jet fuel-range hydrocarbon biofuels.

The idea of the aforementioned carbon–carbon coupling reaction was pioneered by Huber's and Dumesic's groups.^{11,12} Their research groups first reported multi-step reactions to produce hydrocarbon biofuels from carbohydrates. Their process includes dehydration of sugars to furfural/5-hydroxymethylfurfural (5-HMF), conversion of furfural/5-HMF by the aldol-condensation reaction with acetone, and dehydration/hydrogenation of the condensed product. Recently, Corma *et al.* and Zhang *et al.* reported a new pathway for hydrocarbon biofuels from furanic platform chemicals.^{13,14} This process involves the HAA reaction between a carbonyl compound (furfural/5-HMF) with α -hydrogen-containing furan (2-MF), followed by HDO of the high molecular weight fuel precursors (Scheme 1). The α -hydrogen-containing furanic platform chemical, furfural, however, exhibited no reactivity with carbonyl compounds owing to the existence of the electronegative aldehyde group attached to the furan ring. The protective methyl group in the furanic structure of 2-MF, however, makes it very much reactive for HAA reaction. Therefore, the HAA reaction of 2-MF was investigated with numerous carbonyl compounds, for instance, furfural, 5-HMF, butanal, acetone, angelica lactone, ethyl levulinate, mesityl oxide, acetoin, and hydroxyl acetone.^{13–22} Furthermore, 2-MF was oligomerized to a trimer followed by HDO to produce diesel-range biofuel.²³

HAA reaction proceeds in the presence of both homogeneous and heterogeneous acid catalysts.^{18,24} Homogeneous acid catalysts are, however, unsuitable for industrial processes owing to their corrosiveness and complexity in separation and

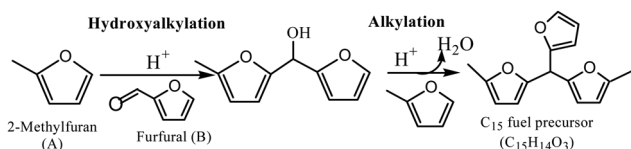
recycling. On the contrary, the solid-acid catalysts can be easily separated from the reaction mixtures and reused. The solid-acid catalysts, such as heteropolyacids, zeolites, acidic resins, and functionalized metal oxides, were thus widely used for this reaction.^{20,25} Among these, acidic resins demonstrated high catalytic activity with a stable catalytic performance towards HAA reaction.^{25,26} Nafion-212 displayed the maximum catalytic activity with 75% 2-MF conversion and a 67% carbon yield under mild reaction conditions.^{14,25} The sulfonated nanostructured carbon showed more than 90% 2-MF conversion.²⁷ In this study, the HAA reaction of furfural with 2-MF was investigated using a cation exchange resin (CER) as the catalyst. The role of various reaction variables, such as CER loading, reaction temperature, and 2-MF/furfural ratio, were further studied to obtain optimum reaction conditions. An appropriate kinetic model was further proposed to validate the experimental data.

HDO of the fuel precursors obtained by HAA reaction was reported over C, SiO₂, and SiO₂–Al₂O₃ supported noble metal (Pd, Pt, Ru, *etc.*) catalysts.^{14,18,28} The Pt/ZrP showed the best catalytic activity with a 94% carbon yield and C₁₅ alkane as the primary product.¹⁴ The noble metal-based catalysts are, however, costly with limited industrial applications. The focus has been shifted to bifunctional catalysts for one-pot synthesis of fuel-range alkanes, such as Pd loaded NbOPO₄/SBA-15, Nb₂O₅/SBA-15, and FeO_x/SiO₂ and Ru/HAP combined with HZSM-5.^{29–31} However, the multifunctional catalysts involve complex preparation methods.³² Recently, a new strategy of mechanical mixing of acid catalysts with supported metal catalysts was assessed.^{32,33} In the present study, we proposed a γ -Al₂O₃ supported low-cost transition metal, nickel, as the catalyst for HDO of the C₁₅ fuel precursor. The extensive characterization of the catalysts was performed to establish the structure-catalytic activity relation. The understanding of the reaction mechanism is of profound importance in designing suitable catalysts for HDO reaction and to obtain desired hydrocarbons by tuning appropriate process parameters. However, the comprehensive mechanistic study of HDO of the C₁₅ fuel precursor is limited in the published literature. The examination of the HDO reaction mechanism for the C₁₅ fuel precursor is thus another objective of the present study. A systematic experimental investigation was carried out for HDO of the C₁₅ fuel precursor over Ni/ γ -Al₂O₃ catalysts with different Ni metal contents on γ -Al₂O₃ under a wide range of temperatures and hydrogen partial pressures. The detailed quantification of individual hydrocarbons and oxygenated intermediate compounds were carried out to corroborate a suitable HDO reaction mechanism.

2. Experimental

2.1 Preparation of catalysts

The Ni/ γ -Al₂O₃ catalysts were synthesized by the incipient wetness impregnation method. At first, a saturated solution of the requisite amount of nickel nitrate hexahydrate (99% purity, Loba Chemie) was prepared using deionized water. The saturated solution of the precursor was then added to γ -Al₂O₃



Scheme 1 Hydroxyalkylation–alkylation reaction of 2-MF with furfural.



and mixed continuously for two hours. The resulting wet catalyst was dried for twelve hours in an oven at 373 K and calcined at 823 K for six hours. This catalyst was referred to as the calcined catalyst. The NiO/ γ -Al₂O₃ (calcined) catalyst was finally activated by reduction using hydrogen at 923 K for six hours. The obtained catalyst was denoted as the reduced catalyst. The catalyst with *x* wt% Ni metal on γ -Al₂O₃ was denoted as *x*NiAl.

2.2 Characterization of the catalysts

The specific surface areas and pore-volumes of the Ni/ γ -Al₂O₃ catalysts were obtained from multipoint nitrogen adsorption-desorption isotherms (77 K) using the Brunauer-Emmett-Teller (BET) equation and Barret-Joyner-Halenda (BJH) method, respectively (Micromeritics, ASAP 2020 system). The catalysts were initially degassed at 623 K for three hours under a vacuum to remove moisture, impurities, and adsorbed gases. The adsorption isotherm was measured by the gradual rise of partial pressure of nitrogen up to the saturation pressure for complete adsorption of nitrogen on the catalyst. The desorption isotherm was then measured by reducing the partial pressure of nitrogen slowly to desorb nitrogen from the catalyst. Temperature-programmed reduction (TPR), temperature-programmed desorption of ammonia (NH₃-TPD), and pulse chemisorption experiments were performed using an Autochem II 2920, Micromeritics system. The instrument was equipped with TCD for continuous monitoring of hydrogen consumption and NH₃ desorption during the experiment. TPR study elucidates the presence of reducible species, reduction temperature, ease of reduction, and interaction between different species. For the TPR study, the metal oxide catalyst (calcined) was first pretreated at 523 K for one hour with argon (20 ml per min) to remove moisture and adsorbed gases and then cooled to room temperature. Following pretreatment, the catalysts were exposed to 10 vol% H₂ in Ar (50 ml per min), and the temperature was then raised linearly from room temperature to 1223 K with a 10 K per min heating rate. The amount of hydrogen consumed in the TPR study was calculated from the peak area using pulse calibration data. For hydrogen pulse chemisorption, the reduction of the metal oxide catalyst (calcined) was first performed at 923 K under a flow of 10 vol% H₂ in Ar (20 ml per min). The reduced catalyst was then flushed with Ar (20 ml per min) with simultaneous cooling up to 323 K. Following cooling, successive pulses of 10 vol% H₂-Ar were introduced. The pulses were continued until the complete chemisorption of hydrogen. The percentage dispersion of nickel and nickel surface area per g nickel were estimated using the quantity of chemisorbed hydrogen. NH₃-TPD discloses the acidity of the catalyst and its strength. The catalyst was first degassed at 523 K for one hour under an Ar flow (10 ml per min) and then cooled to 323 K. Ammonia (20 ml per min) was then introduced at 323 K and equilibrated for 30 min. The physisorbed ammonia was then removed by sending Ar (50 ml per min) for one hour, and the catalyst was then heated linearly up to 1073 K with 10 K per min heating rate to quantify the desorbed ammonia at different temperatures. The powder

X-ray diffraction (XRD) pattern of the NiO/ γ -Al₂O₃ and Ni/ γ -Al₂O₃ catalysts was obtained using a Rigaku smart lab X-ray diffractometer at 2θ of 10°–90° and 2° per min scanning rate. The morphological information was obtained by transmission electron microscopy (TEM) using a JEOL JEM 2100FX system with a filament of LaB₆ at 200 kV. The fine powder sample was first dissolved in ethanol using ultrasonication for 2 h. One drop of the prepared specimen was then deposited on a carbon-coated grid and the ethanol was evaporated before analysis.

2.3 Hydroxyalkylation-alkylation (HAA) reaction study

HAA reaction was investigated in a batch-reactor assembly consisting of a round bottom flask, condenser, and magnetic stirrer. The reactor was submerged in a temperature-controlled oil bath. The oil bath was placed on the hot plate of a magnetic stirrer. A PID controller was used to control the temperature of the oil bath. After the attainment of the set point temperature of the oil bath, known quantities of furfural (98% purity, Alfa Aesar), 2-MF (>98% purity, Alfa Aesar), and a CER catalyst (min 4.5 meq per g, Sisco Res. Lab. Pvt. Ltd) were charged into the round bottom flask and stirred at a constant stirring speed. The reaction samples were acquired at different time intervals. These samples were filtered using a syringe filter and diluted with 1-octanol (external standard, Spectrochem Pvt. Ltd, 98% purity). The products were identified by GC-MS (Shimadzu, GC-2010 system) and quantified by GC-FID using nitrogen as the carrier gas (Fig. S1, ESI†).

2.4 Hydrodeoxygenation (HDO) reaction of C₁₅ fuel precursor

The C₁₅ fuel precursor was first prepared by the HAA reaction of 2-MF with furfural using the CER catalyst with excess 2-MF under otherwise optimal reaction conditions. The reaction mixture was filtered to separate the CER catalyst and then diluted with acetone. The unreacted reactants (mainly 2-MF) and acetone were then removed from the product mixture using a rotary evaporator to obtain the C₁₅ fuel precursor with more than 95% purity. HDO of the C₁₅ fuel precursor was then carried out at high hydrogen pressure in a stirred autoclave reactor. The reactor was heated using an electrical heater, whose temperature was maintained at ± 1 K of a set point temperature using a PID controller. At first, 3 g of C₁₅ fuel precursor, 69 g of *iso*-octane (solvent and internal standard, Sisco Res. Lab. Pvt. Ltd, 99% purity), and a measured quantity of Ni/ γ -Al₂O₃ catalyst were loaded into the reactor. The air from the reactor was removed by hydrogen flushing for about 10 min. The pressure of the reactor was then raised using hydrogen, and the reactor was heated to the set point temperature, while maintaining a constant stirring speed of 1000 rpm. The high agitation speed was maintained to eradicate the external mass transfer resistance in this reaction. After attaining the set point temperature, the first sample was acquired, and it was designated as the initial (zero min) reaction sample. Additional reaction mixtures were acquired at several time intervals. The collected samples were first quenched with acetone, and the suspended catalyst particles were then separated using a centrifuge. The identification of the chemical



formulae and quantification of the products were then performed by GC-MS and GC-FID, respectively, using a ZB-5HT capillary column (30 m × 0.32 mm × 0.10 μm) and nitrogen as the carrier gas. The oven temperature was initially kept at 313 K for five minutes, increased to 498 K with a ramp rate of 30 K per min, maintained there for two minutes, then raised to 508 K with a heating rate of 20 K per min, and held there for four minutes. The detector and injector were kept at 653 K and 613 K, respectively. Following the completion of the reaction, the gas-phase samples were analysed by GC-FID (Fig. S2, ESI†) and GC-TCD (Fig. S3, ESI†) to examine the possible formation of volatile hydrocarbons and gases.

3. Results and discussion

3.1. Hydroxyalkylation-alkylation reaction

The 2-MF conversion was only about 20% at 300 min of reaction time for 0.5 g of the CER loading (Fig. 1A). The 2-MF conversion

was, however, increased to around 39% by raising the CER loading to 1.0 g. The enhanced catalytic activity of the CER was because of the rise in catalytically active acid sites. The 2-MF conversion was, however, not increased much by increasing the catalyst loading to 1.5 g owing to the presence of excess catalytic sites than required for the reaction. The CER loading of 1.0 g was thus considered as the optimum. In our study, the intermediate products from the hydroxyalkylation reaction were not observed (Scheme 1). This might be due to the slower rate of hydroxyalkylation reaction than the alkylation reaction.²⁷ The hydroxyalkylation reaction was thus considered as the rate-determining step in the kinetic model. Moreover, we observed only small quantities of other products (less than 1%), especially at longer reaction times. These products were, therefore, excluded from the results. All reactions were studied at a high agitation rate to eliminate the external mass transfer resistance. The reaction was assumed to be first order for both the reactants: 2-MF (A) and furfural (B). Accordingly, the rate of

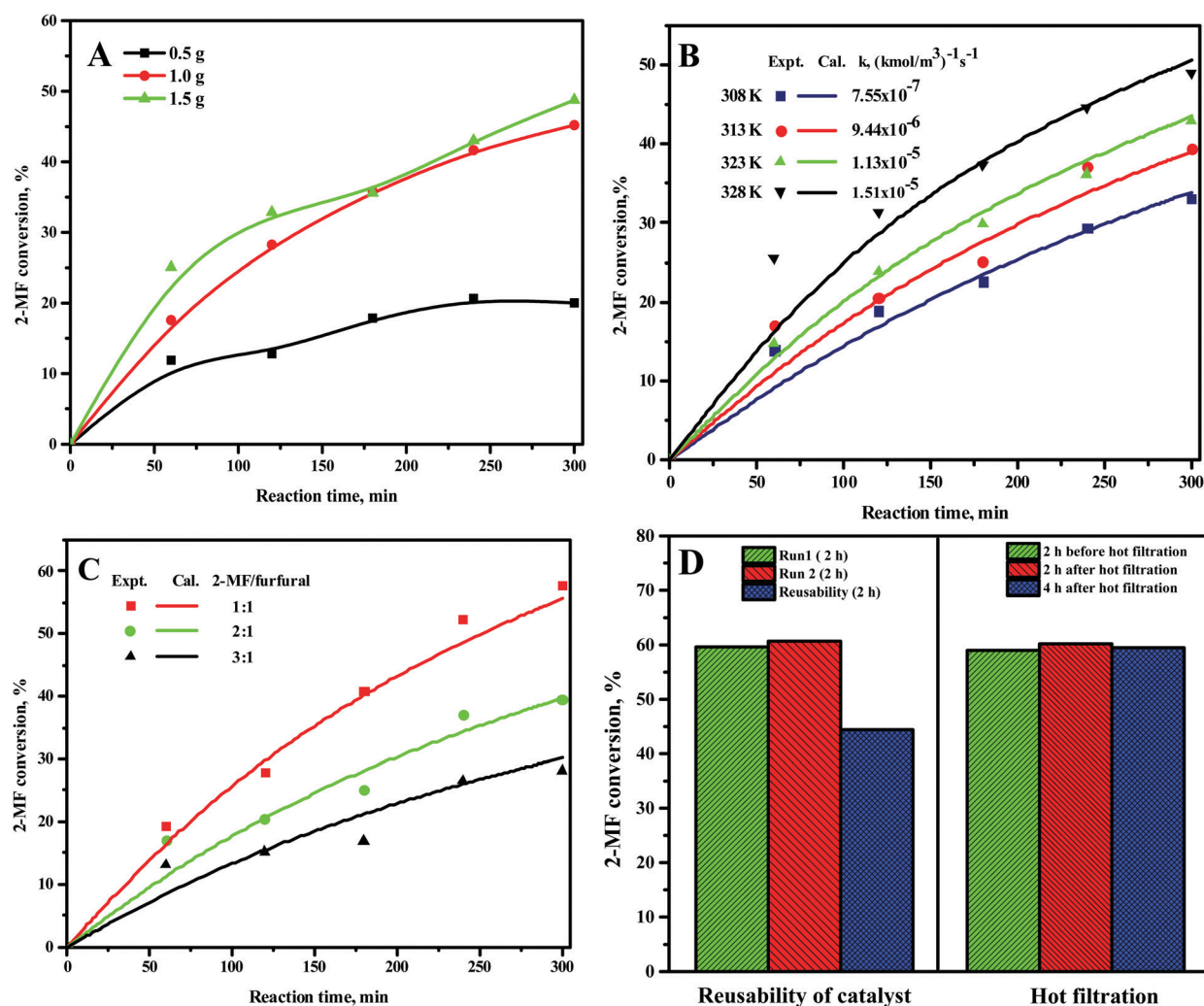


Fig. 1 Effect of (A) CER loading, (B) reaction temperature, and (C) 2-MF/furfural mole ratio on 2-MF conversion, and (D) reusability and hot filtration study. Reaction conditions: (A) 0.1997 mol 2-MF, 0.1004 mol furfural, and 313 K. (B) 0.1997 mol 2-MF, 0.1004 mol furfural, and 1 g CER. (C) 313 K and 1 g CER. (D) 328 K, 1.5 g CER, and 2 : 1 2-MF/furfural.



formation of A was expressed by the following rate equation considering X as the conversion of A and θ_B as the ratio of initial moles of B to that of A (C_{B0}/C_{A0}).

$$\frac{dC_A}{dt} = -kC_A C_B \dots \therefore \frac{dX}{dt} = kC_{A0}(1-X) \left(\theta_B - \frac{X}{2} \right) \quad (1)$$

The following equation was obtained after integrating the above equation.

$$\ln \frac{\theta_B(1-X)}{\left(\theta_B - \frac{X}{2}\right)} = \frac{C_{A0}(1-2\theta_B)kt}{2} \quad (2)$$

$$\therefore X = 2\theta_B \frac{(1 - e^{ktC_{A0}(1-2\theta_B)/2})}{(2\theta_B - e^{ktC_{A0}(1-2\theta_B)/2})}$$

The kinetic study for the HAA reaction was executed in the temperature range of 308–328 K (Fig. 1B). The 2-MF conversion at 6 h of reaction time was around 33% at 308 K and enhanced to about 39%, 42%, and 49% at 313 K, 323 K, and 328 K, respectively. The experimental $\ln \frac{\theta_B(1-X)}{\left(\theta_B - \frac{X}{2}\right)}$ vs. time (t) data at

different temperatures fitted well by linear lines passing through the origin (Fig. S4, ESI†). This result confirms that the reaction is second order. The rate constant of this reaction was calculated at different temperatures from the slope of $\ln \frac{\theta_B(1-X)}{\left(\theta_B - \frac{X}{2}\right)}$ vs. time (t) (Fig. 1B). The 2-MF conversion was

then estimated based on eqn (2) using the calculated rate constants at various reaction temperatures and matched with 2-MF conversions obtained from experiments. 2-MF conversions calculated using the above kinetic model fitted very well with the experimental 2-MF conversions, as observed from the figure. The activation energy ($15.09 \text{ kcal mol}^{-1}$) and pre-exponential factor ($1.8 \times 10^5 \text{ (kmol m}^{-3}\text{)}^{-1} \text{ s}^{-1}$) were further obtained from the Arrhenius plot of $1/\text{temperature}$ vs. $\ln(k)$ (Fig. S5, ESI†). The high activation energy further elucidates the absence of external mass transfer resistance. The study was then extended to various 2-MF/furfural mole ratios to validate the established kinetic model. The 2-MF conversion was decreased with the increase in the 2-MF/furfural molar ratio from 1:1 to 3:1 (Fig. 1C).²⁷ For different 2-MF/furfural mole ratios, the 2-MF conversions were estimated using the calculated rate constants at 313 K and compared with the 2-MF conversions obtained from experiments. The calculated 2-MF conversions for various 2-MF/furfural molar ratios matched the corresponding experimental 2-MF conversions quite well.

The reproducibility study was further performed under identical reaction conditions, and the reaction results were found to be reproducible (Fig. 1D). The spent CER from these reactions was separated, washed with ethanol, and then dried at 373 K overnight. The activity of the spent CER was tested under the same reaction conditions. The spent CER exhibited a slightly lower 2-MF conversion compared to the fresh catalyst (Fig. 1D). The hot-filtration test was further performed to check

the possible catalyst deactivation by leaching of $-\text{SO}_3\text{H}$ groups. The reaction was initially carried out for two hours, the catalyst was separated from the reaction mixture under hot conditions, and the reaction was then continued for an additional four hours without the catalyst. However, the conversion of 2-MF remained unchanged after hot filtration. This result eliminates the possibility of deactivation of CER by leaching of $-\text{SO}_3\text{H}$ groups. The optimum HAA reaction conditions were found to be 1 g CER loading, 1:1 2-MF/furfural, and 328 K. About 66% 2-MF conversion and 96% selectivity towards C_{15} fuel precursor was observed under the optimum conditions at 5 h of reaction time. However, the C_{15} fuel precursor was prepared using 2:1 2-MF/furfural mole ratio (0.43 mol 2-MF and 0.21 mol furfural) under otherwise optimum reaction conditions. The conversion of furfural was more than 95% under these reaction conditions. A slight excess of 2-MF was used for the preparation of the C_{15} fuel precursor for an easy elimination of excess volatile 2-MF from the reaction mixture after the reaction.

3.2. Characterization of the Ni/ γ - Al_2O_3 catalysts

The specific surface area and pore volume of both the NiO/ γ - Al_2O_3 (calcined) and Ni/ γ - Al_2O_3 (reduced) catalysts were lower than those of γ - Al_2O_3 (Table 1). Moreover, the specific surface area and pore volume of these catalysts was decreased with increasing Ni metal content on γ - Al_2O_3 .^{34,35} This was due to the blockage of γ - Al_2O_3 pores and coverage of the γ - Al_2O_3 surface by Ni/NiO particles. It was further observed that the Ni/ γ - Al_2O_3 (reduced) catalysts exhibited a lower specific surface area than the NiO/ γ - Al_2O_3 (calcined) catalysts. This might be due to the agglomeration/sintering of nickel metal during high-temperature reduction at 973 K.

TPR study exhibited three distinct reduction peaks for NiO/ γ - Al_2O_3 (calcined) catalysts at 590–618 K, 670–685 K, and 700–850 K (Fig. 2A).³⁴ The bulk NiO showed a reduction peak at 618 K. The NiO/ γ - Al_2O_3 catalysts also displayed a similar reduction peak at 590–618 K. The lowest temperature reduction peak for the NiO/ γ - Al_2O_3 catalysts was thus assigned to bulk NiO having a weak interaction with the γ - Al_2O_3 support. The peak observed at 670–685 K corresponded to the dispersed NiO reduction. The interaction of dispersed NiO with the γ - Al_2O_3 support was slightly stronger compared to that of bulk NiO. The strong metal-support interaction for dispersed NiO was reflected by the slightly higher reduction temperatures. The reduction peak at 700–850 K was associated with NiAl_2O_4 species.³⁴ This species has the strongest interaction with the support with the highest reduction temperature. The hydrogen consumption was further calculated from TPR experiments, as shown in Table 1. The hydrogen consumption was improved with the growing nickel metal content on γ - Al_2O_3 . However, the degree of NiO reduction was slightly lower for higher nickel metal content on γ - Al_2O_3 . The dispersion of nickel and nickel surface area per gm nickel were reduced slightly for rising Ni metal content on γ - Al_2O_3 (Table 1).³⁴ This was due to the increased amount of bulk NiO with increasing Ni metal content on γ - Al_2O_3 (Fig. 2A).



Table 1 Physicochemical properties of the Ni/ γ -Al₂O₃ catalysts

Catalyst	BET		Chemisorption		dc, nm		Acidity, mmol g ⁻¹		TPR		
	cal		red		MD	SM	cal (NiO)	red (Ni)	red	MH2	DR
	SSA	PV	SSA	PV							
γ -Al ₂ O ₃	237	0.83	—	—	—	—	—	—	NIL	—	—
10NiAl	198	0.61	180	0.63	1.16	7.74	13.8	10.53	0.15	1.32	77.5
15NiAl	193	0.60	177	0.64	0.90	6.00	14.24	12.37	0.39	1.78	69.8
20NiAl	189	0.59	169	0.62	0.80	5.45	14.59	14.04	0.50	2.41	71.1
25NiAl	169	0.52	156	0.55	0.77	5.17	19.16	20.04	0.44	2.84	66.7
20NiAl (spent)	—	—	142	0.59	0.62	4.38	—	20.65	0.43	2.10	62.0

red = Reduced catalyst; cal = calcined catalyst; PV = pore volume, cm³ g⁻¹; SSA = specific surface area, m² g⁻¹; MD = dispersion of nickel, %, SM = nickel surface area, m² g⁻¹ nickel; dc = Ni/NiO crystallite size; MH2 = mmol of H₂ consumed per g catalyst; DR = degree of reduction of NiO, %.

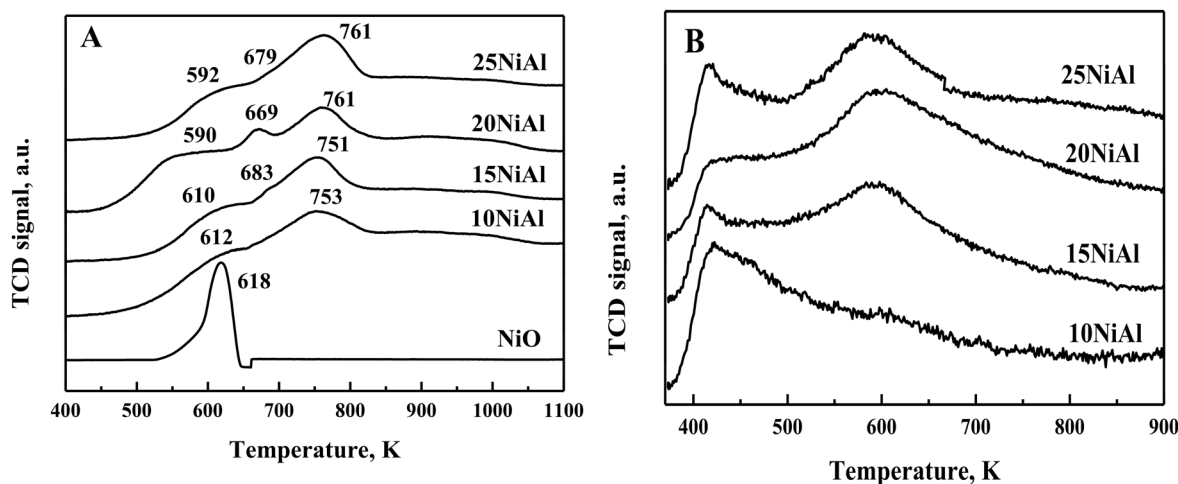


Fig. 2 (A) TPR profiles of the bulk NiO and NiO/ γ -Al₂O₃ (calcined) catalysts. (B) NH₃-TPD profiles of the Ni/ γ -Al₂O₃ (reduced) catalysts.

The NH₃-TPD results exhibited two types of acid sites for the Ni/ γ -Al₂O₃ (reduced) catalysts (Fig. 2B). The first NH₃ desorption peak at a lower temperature (400–517 K) represents the weak acid sites. These acid sites were due to the surface hydroxyl groups.³⁶ The second NH₃ desorption peaks at 517–678 K represent the moderate acid sites. The under-coordinated Lewis acidic aluminium cations were responsible for these acid sites.³⁶ The moderate acid sites were absent in the 10 wt% Ni/ γ -Al₂O₃ catalyst. Besides, the intensity of the moderate acid sites was increased with rising Ni metal content on γ -Al₂O₃ from 15 to 25 wt%. The total acidity was calculated from these NH₃ desorption peaks, as shown in Table 1. The total acidity was increased with rising Ni metal content on γ -Al₂O₃ up to 20 wt% and decreased slightly for 25 wt%. This was due to a slight decrease in moderate acid sites for 25 wt% Ni/ γ -Al₂O₃. The drop in acidity for 25 wt% nickel metal content on γ -Al₂O₃ was owing to the existence of a large amount of bulk NiO, as observed from the TPR results (Fig. 2A).

The powder XRD pattern of both the NiO/ γ -Al₂O₃ (calcined) and Ni/ γ -Al₂O₃ (reduced) catalysts with various Ni metal contents on γ -Al₂O₃ are presented in Fig. 3. The powder XRD pattern of the bulk NiO and support (γ -Al₂O₃) were additionally acquired to distinguish the diffraction peaks corresponding to

NiO and γ -Al₂O₃. The NiO diffraction peaks for the NiO/ γ -Al₂O₃ catalyst were observed at 2θ of 37.28° (1 1 1), 43.28° (2 0 0), and 62.87° (2 2 0). Similarly, the Ni/ γ -Al₂O₃ (reduced) catalysts revealed the Ni species at 2θ of 37.09° (1 1 1) and 44.30° (2 0 0). The crystallite size of the catalysts was also determined using the Scherrer equation, as shown in Table 1. The NiO and Ni crystallite sizes were enlarged with the rising nickel metal contents on γ -Al₂O₃ for the calcined and reduced catalysts, respectively. The enlarged Ni crystallite sizes resulted in a drop in nickel dispersion and the nickel surface area per g nickel (Table 1).

3.3. Reaction mechanism for HDO of the C₁₅ fuel precursor

The C₁₅ fuel precursor is a complex chemical compound with multiple functionalities. The reaction mechanism for HDO of such a complex molecule is thus quite intricate. In this study, we made an effort to delimit a possible HDO reaction mechanism to elucidate the product distribution over a wide range of reaction conditions. C₉–C₁₅ alkanes were detected as the hydrocarbon products over the Ni/ γ -Al₂O₃ catalysts (Fig. 4). We also perceived a trivial quantity of greater than C₁₅ alkanes during this study. However, the C₁₃–C₁₅ alkanes were the leading hydrocarbon products, with C₁₄H₃₀ being the dominant one.



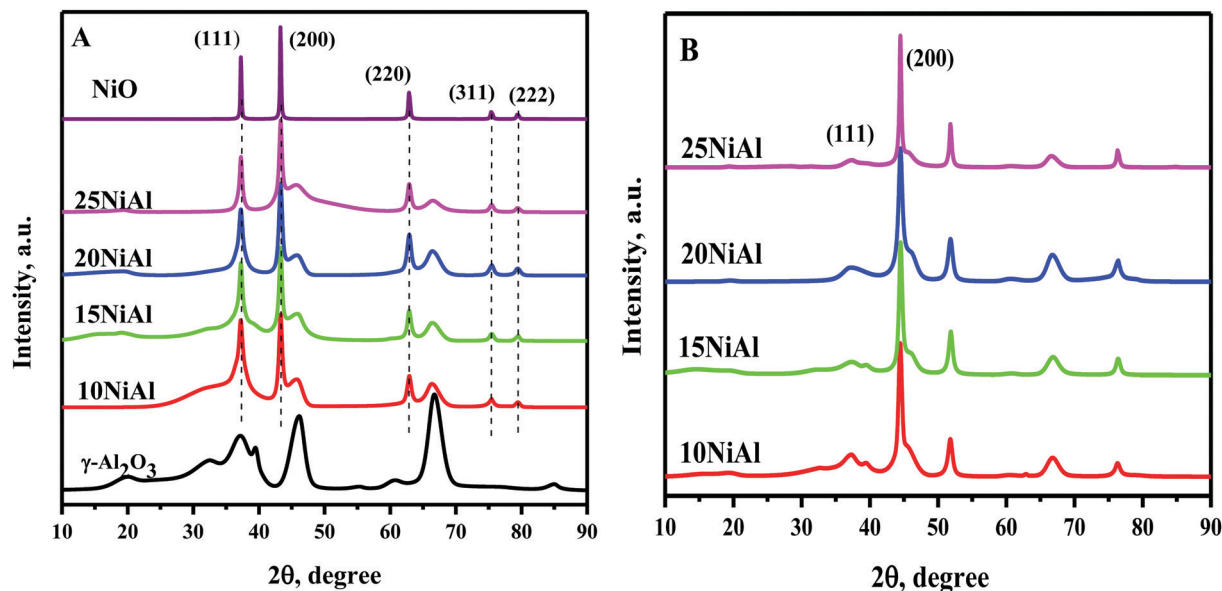


Fig. 3 Powder XRD pattern of the (A) Ni/ γ -Al₂O₃ (calcined) and (B) Ni/ γ -Al₂O₃ (reduced) catalysts.

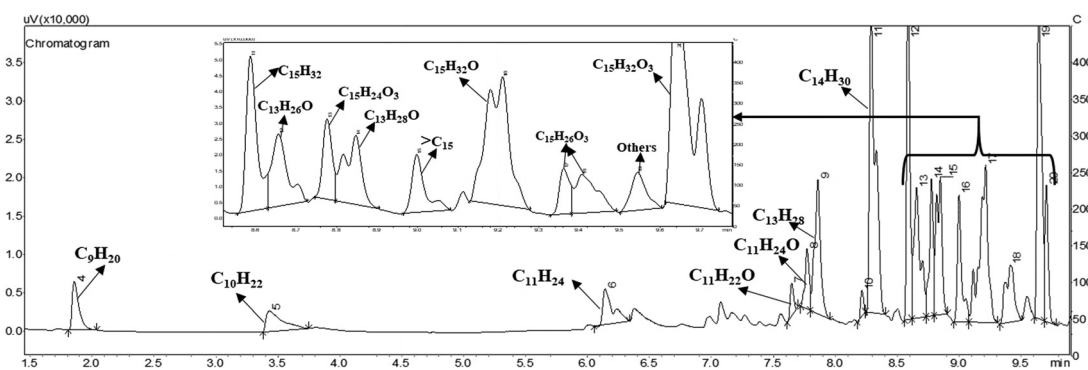


Fig. 4 A typical GC chromatogram for HDO of the C₁₅ fuel precursor. Reaction conditions: 0.5 g 20NiAl, 573 K, 15 min of reaction time, and 30 bar H₂.

Besides, many oxygenated intermediate compounds were perceived. However, the GC peaks of these oxygenated intermediate compounds were overlapping, posing a great difficulty in their clear identification. The chemical formulae of a few of these oxygenated intermediate compounds were identified, as shown in Fig. 4 and Fig. S6 (ESI[†]).

Typical concentration profiles for hydrocarbons and oxygenated intermediate compounds are displayed in Fig. 5. The C₁₅ fuel precursor was not detected in the initial (zero min) reaction sample. On the contrary, a high wt% of C₁₅H₂₆O₃ (I) was observed in the initial reaction sample (Scheme 2). Furthermore, the wt% C₁₅H₂₆O₃ (I) was declined rapidly with the progress of the reaction. These results revealed that the furan ring hydrogenation was the initial step of the reaction. Liu *et al.* observed three isomers of C₁₅H₂₆O₃ as the major products during the initial reaction time.³⁷ We further observed GC peak splitting for C₁₅H₂₆O₃. Therefore, we cannot disregard the possibility of these isomers completely. Furthermore, XIV–XVI

compounds in Scheme 2 bear the same chemical formula, C₁₅H₂₆O₃. The furan rings generally undergo sequential hydrogenation of individual double bonds. However, we detected only a trivial amount of a partial ring hydrogenation product (C₁₅H₂₄O₃) during this study. Dutta *et al.* observed partial and complete furan ring hydrogenation products only at 298 K and 50 bar hydrogen pressure over the Pd/C-Hf(OTf)₄ catalyst.³⁸ However, the furan ring hydrogenation products were absent at 498 K with the concurrent appearance of furan ring-opening products. The furan ring hydrogenation reaction occurs on metallic sites. Therefore, this reaction was rapid over the Ni/ γ -Al₂O₃ catalyst with a high wt% of complete furan ring hydrogenation product (C₁₅H₂₆O₃, I) at the initial reaction time. On the other hand, furan ring-opening products were absent in the initial reaction sample. These results endorse the faster rate of furan ring hydrogenation than the ring-opening reaction under the prevailing reaction conditions. The furan ring hydrogenation was reported to be competitive with the furan



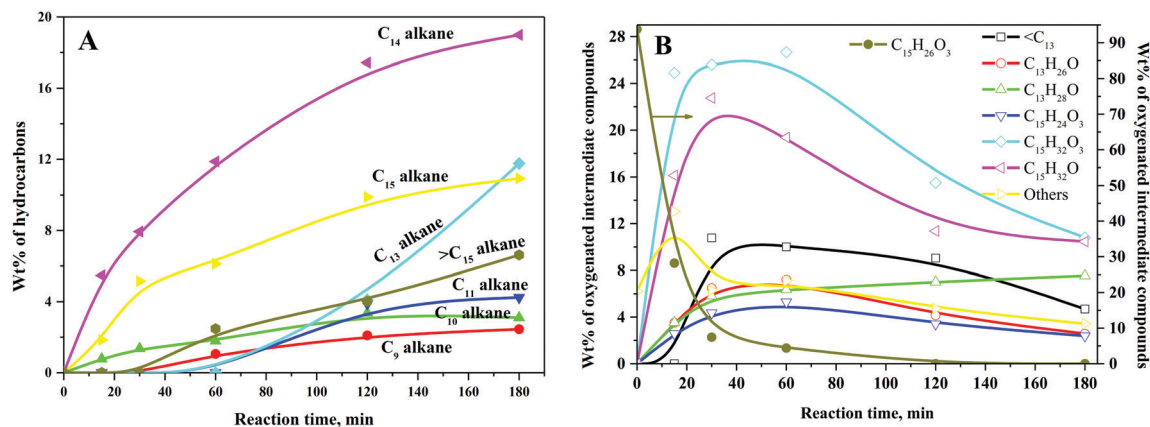
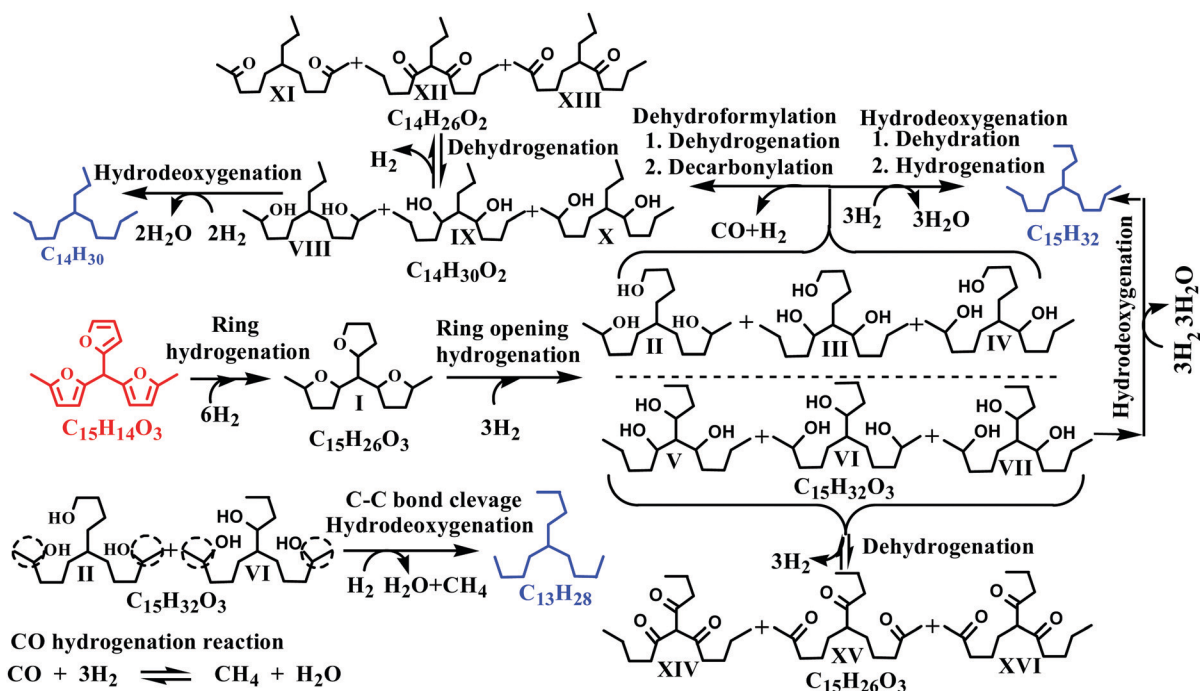


Fig. 5 Typical concentration profiles of (A) hydrocarbons and (B) oxygenated intermediate compounds for HDO of the C_{15} fuel precursor. Reaction conditions: 0.5 g 20NiAl, 543 K, and 30 bar H_2 .



Scheme 2 Proposed reaction mechanism for hydrodeoxygenation of the C_{15} fuel precursor.

ring-opening reaction at high hydrogen pressure.³⁹ Besides, the hydrogenation of double bonds of furan was reported to be thermodynamically favorable with the formation of tetrahydrofuran.⁴⁰ The furan ring hydrogenation product was found to be dominant during HDO of 2,5-dimethylfuran.^{37,38,41}

We observed a noticeable quantity of $C_{15}H_{32}O_3$ isomers (II–VII) at 15 min of reaction time. The wt% of this product was further increased up to 30 min of reaction time and decreased gradually beyond this reaction time. $C_{15}H_{32}O_3$ isomers (II–VII) were formed by the furan ring opening of the full ring hydrogenation product ($C_{15}H_{26}O_3$, I) of the C_{15} fuel precursor. The formation of the $C_{15}H_{32}O_3$ (II–VII) isomers was

reflected by the splitting of the corresponding GC peaks (Fig. 4). However, we could not confirm the formation of partial furan ring opening compounds. The furan ring opening isomers ($C_{15}H_{32}O_3$, II–VII) subsequently underwent deoxygenation following two primary reaction routes: dehydroformylation and HDO. The three isomers of $C_{15}H_{32}O_3$ (II–IV) have a terminal hydroxyl (OH) group. Following the former route, these $C_{15}H_{32}O_3$ (II–IV) isomers followed dehydroformylation reaction, *i.e.*, dehydrogenation, followed by decarbonylation, to form $C_{14}H_{30}O_2$ (VIII–X). This route was endorsed by the formation of CO in the gas-phase (Fig. S3, ESI[†]). Palla *et al.* studied the HDO of aliphatic alcohols with the terminal OH group over



the Ni/ γ -Al₂O₃ catalyst and observed alkanes and alkenes with one carbon less than the alcohols as the product.⁴² These products were reported to be formed by dehydrogenation, followed by either decarbonylation or dehydroformylation reactions.⁴² The C₁₄H₃₀O₂ (VIII–X) isomers then underwent HDO, *i.e.*, dehydration, followed by hydrogenation reaction, to form C₁₄H₃₀. The C₁₄H₃₀O₂ (VIII–X) isomers can also undergo the dehydrogenation reaction to form the corresponding ketones. Yang *et al.* reported the HDO of 5-nonanone using aluminosilicate supported Ni and Co catalysts, and perceived 5-nonanol as the intermediate product.⁴³ The HDO reaction was proposed to follow *via* hydrogenation to 5-nonanol, followed by dehydration and hydrogenation reaction. HDO of 2-hexanone and 3-hexanone was reported to follow *via* initial hydrogenation to the corresponding alcohols.⁴⁴ These alcohols then underwent HDO following dehydration and hydrogenation reaction. The dehydrogenation of C₁₄H₃₀O₂ (VIII–X) isomers to the corresponding C₁₄H₂₆O₂ (XI–XIII) compounds was thus considered a reversible reaction.

Following the latter route (HDO), the C₁₅H₃₂O₃ (II–VII) isomers underwent deoxygenation through dehydration, followed by the hydrogenation reaction, forming C₁₅H₃₂ alkane. The C₁₅H₃₂O₃ (V–VII) compounds can also undergo a reversible dehydrogenation reaction to the corresponding ketones (XIV–XVI). The dehydroformylation reaction occurs over metallic centers of the catalyst, while acidic sites are responsible for the HDO reaction. The Ni/ γ -Al₂O₃ is a weakly acidic metal catalyst (Table 1 and Fig. 2B). The dehydroformylation reaction was thus relatively faster compared to the HDO reaction over the Ni/ γ -Al₂O₃ catalyst with C₁₄ alkane as the dominant hydrocarbon. The dehydroformylation reaction was also reported to be dominant for the C₁₅ fuel precursor over the Pd/C-Hf(OTf)₄ catalyst, with C₁₄ alkane as the leading product.³⁸ Li *et al.* studied the HDO of the C₁₄ fuel precursor derived from 2-MF and butanal by the HAA reaction over zeolite (HZSM-5 and HMOR)-supported nickel as a bifunctional (metal and acid) catalyst.¹⁹ The HDO reaction was found to be the dominant route, with C₁₄ alkanes as the major product.

We further studied the HDO of 2-octanol over the Ni/ γ -Al₂O₃ catalyst to explore the HDO reaction mechanism of secondary alcohols. *n*-Octane was found to be the primary product with only a small amount of *n*-heptane and 2-octanone. We envisioned the formation of *n*-heptane by the cracking reaction of the terminal carbon–carbon bond attached to the OH group. Based on these results, we proposed the terminal carbon–carbon bond cleavage of C₁₅H₃₂O₃ (II and VI) isomers, followed by HDO of the resulting compounds, to form C₁₃H₂₈ alkane. The wt% of C₁₃ alkane was negligible at the early stages of the reaction and became prominent only after 60 min of reaction time. These results further support the formation of C₁₃ alkane by a relatively slower cracking reaction. Similarly, the C₉–C₁₂ hydrocarbons were not observed up to 30 min of reaction time, and only a trivial quantity of these hydrocarbons appeared at 60 min of reaction time (Fig. 5A). The C₉–C₁₂ hydrocarbons were possibly formed by a cracking reaction at various positions of II–X compounds under severe reaction conditions. The above

hypothesis was further supported by the formation of the cracked oxygenated intermediate compounds (Fig. S4, ESI[†]) and lighter hydrocarbons in the gas-phase (Fig. S2, ESI[†]) under extreme reaction conditions. Li *et al.* reported that the carbon–carbon bond cleavage between the furan moiety and tertiary carbocation was responsible for the formation of lower hydrocarbons by a series of hydrogenation and dehydration reactions.^{45,46} We observed a small quantity of greater than C₁₅ hydrocarbons. These hydrocarbons were perhaps formed by self- or cross-condensation of ketones, followed by HDO of the condensed compounds. Gurbuz *et al.* also reported the condensation of 2-hexanone using palladium-supported ceria-zirconia mixed oxides.⁴⁷ For the C₁₅ fuel precursor, the decarbonylation of ketones could be a possible reaction route for the deoxygenation. Morioka *et al.* reported nickel/N-heterocyclic carbene-mediated decarbonylation of simple aromatic ketones.⁴⁸ However, the success of ketone decarbonylation is limited due to the difficulty in activation of two inert carbon–carbon bonds. The decarbonylation of ketones was thus not included in our proposed HDO reaction mechanism.

3.4. Role of hydrogen partial pressure

HDO of the C₁₅ fuel precursor was carried out at various hydrogen pressures for a fixed total pressure of 30 bar to elucidate the roles of hydrogen partial pressure on the conversion of oxygenates and wt% of hydrocarbons and oxygenated intermediate compounds. At a 20 bar hydrogen pressure, the oxygenate conversion was only about 50% at 180 min of reaction time and increased to about 95% at 180 min of reaction time for both 25 bar and 30 bar hydrogen pressures (Fig. 6A). The enhanced conversion of oxygenates at elevated hydrogen pressures was due to the greater availability of hydrogen for the conversion of oxygenates to hydrocarbons *via* hydrogenation and HDO reaction. Conversely, the wt% of C₁₄ alkane was high at a 20 bar hydrogen pressure and reduced slightly at higher hydrogen pressures (Fig. 6B). However, the wt% of C₁₅ alkane was low at a 20 bar hydrogen pressure and increased significantly at higher hydrogen pressures. While a high pressure is unsuitable for dehydroformylation reaction, the HDO reaction is favorable at a high hydrogen pressure. The wt% of C₁₅ alkane was thus enhanced with increasing hydrogen partial pressure with a concurrent decline in the wt% of C₁₄ alkane. According to Zhang's group, C₁₄H₃₀ alkanes have a high cetane number and low pour point and can be considered as diesel or fuel additives.¹⁷ At a 20 bar hydrogen pressure, the wt% of furan ring hydrogenated products, *i.e.*, C₁₅H₂₄O₃ and C₁₅H₂₆O₃, was quite high and decreased at higher hydrogen pressures (Fig. 6C). However, the combined wt% of furan ring opening products, *i.e.*, C₁₅H₃₂O₃ and C₁₅H₃₂O, was lower at a 20 bar hydrogen pressure compared to 25 and 30 bar (Scheme 2). These results disclosed enhanced furan ring hydrogenation and ring-opening reactions at elevated hydrogen pressures. The cracking reaction is favorable at a low hydrogen pressure. The wt% of the C₈, C₁₀, and C₁₁ oxygenated intermediate compounds was thus quite significant at a 20 bar hydrogen pressure and reduced at higher hydrogen pressures.



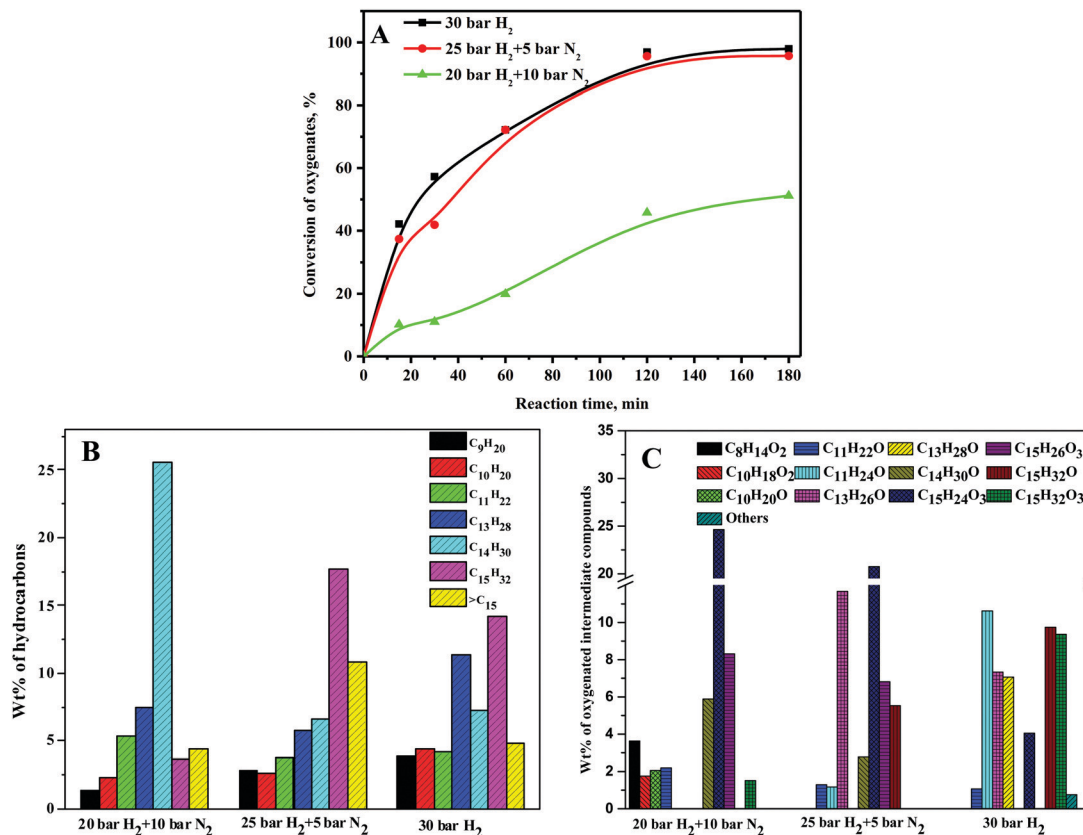


Fig. 6 Role of partial pressure of hydrogen on (A) conversion of oxygenated compounds, (B) wt% of hydrocarbons, and (C) wt% of oxygenated intermediate compounds. Reaction conditions: 0.5 g 20NiAl and 573 K. B and C: 50% conversion of oxygenated compounds.

Since the conversion of oxygenates was not increased much beyond a 25 bar hydrogen pressure, all subsequent studies were carried out at a 30 bar hydrogen pressure.

3.5. Effect of nickel metal content on γ -Al₂O₃

The conversion of the C₁₅ fuel precursor was almost absent in the absence of the catalyst, demonstrating insignificant thermal cracking under the reaction conditions. The reaction was also carried out in the presence of γ -Al₂O₃ to comprehend the role of the support in this reaction. The conversion of the C₁₅ fuel precursor was nearly absent, implying an insignificant role of γ -Al₂O₃ alone for this reaction. The conversion of oxygenates at 5 h of reaction time was about 20% over 10NiAl (Fig. 7A). The conversion of oxygenates was improved with the rising nickel metal content on γ -Al₂O₃ up to 20NiAl and decreased slightly for 25NiAl. The conversion of oxygenates at 300 min of reaction time was about 86% over 20NiAl and dropped to about 76.4% for 25NiAl. The increase in catalytic activity with the rising nickel metal content on γ -Al₂O₃ until 20 wt% was owing to the rise in the amount of metallic sites. This was reflected by the metallic surface area results, *i.e.*, [nickel surface area per g nickel] \times [wt% of nickel] (Table 1). However, a slight decrease in catalytic activity for 25NiAl was due to the existence of a large quantity of catalytically less-active bulk nickel metal species, as observed from the TPR results (Fig. 2).³⁵ The nickel crystallite size was also bigger for 25NiAl compared to 20NiAl (Table 1). Moreover, the acidity of 25NiAl was less compared to 20NiAl (Table 1).⁴⁹

The influence of nickel metal content on γ -Al₂O₃ on the wt% of hydrocarbons and oxygenated intermediate products is displayed in Fig. 7B and C, respectively. C₁₄ alkane was detected as the main hydrocarbon product, followed by C₁₅ and C₁₃ alkane for all the catalysts. The wt% of C₉–C₁₁ alkanes was relatively lower compared to that of C₁₃–C₁₅ alkanes. The cumulative wt% of hydrocarbon products was improved with rising Ni metal content on γ -Al₂O₃ up to 20 wt% (about 86% at 300 min). The wt% values of individual alkane products were, however, not affected much for the increasing nickel metal content on γ -Al₂O₃. It is obvious as the nature of active sites is similar for all the catalysts. Conversely, a vast range of oxygenated intermediate compounds was observed as the products. A significant quantity of C₁₅H₂₆O₃ (I of Scheme 2) was observed for 10NiAl. The wt% of C₁₅H₂₆O₃ was, however, quite small for higher nickel metal content on γ -Al₂O₃. The catalytic activity of the Ni/ γ -Al₂O₃ catalysts was boosted with the growing nickel metal content on γ -Al₂O₃. The low selectivity to C₁₅H₂₆O₃ at 15 wt% and higher nickel content on γ -Al₂O₃ was due to its rapid conversion to C₁₅H₃₂O₃. On the other hand, the wt% of C₁₅H₃₂O₃ was quite significant for all the catalysts. Since 20NiAl showed the highest catalytic activity, all other studies were carried out in the presence of 20NiAl.

3.6. Effect of reaction temperature

The conversion of oxygenates was boosted by the elevation of the reaction temperature, as shown in Fig. 8A. At 4 h of reaction



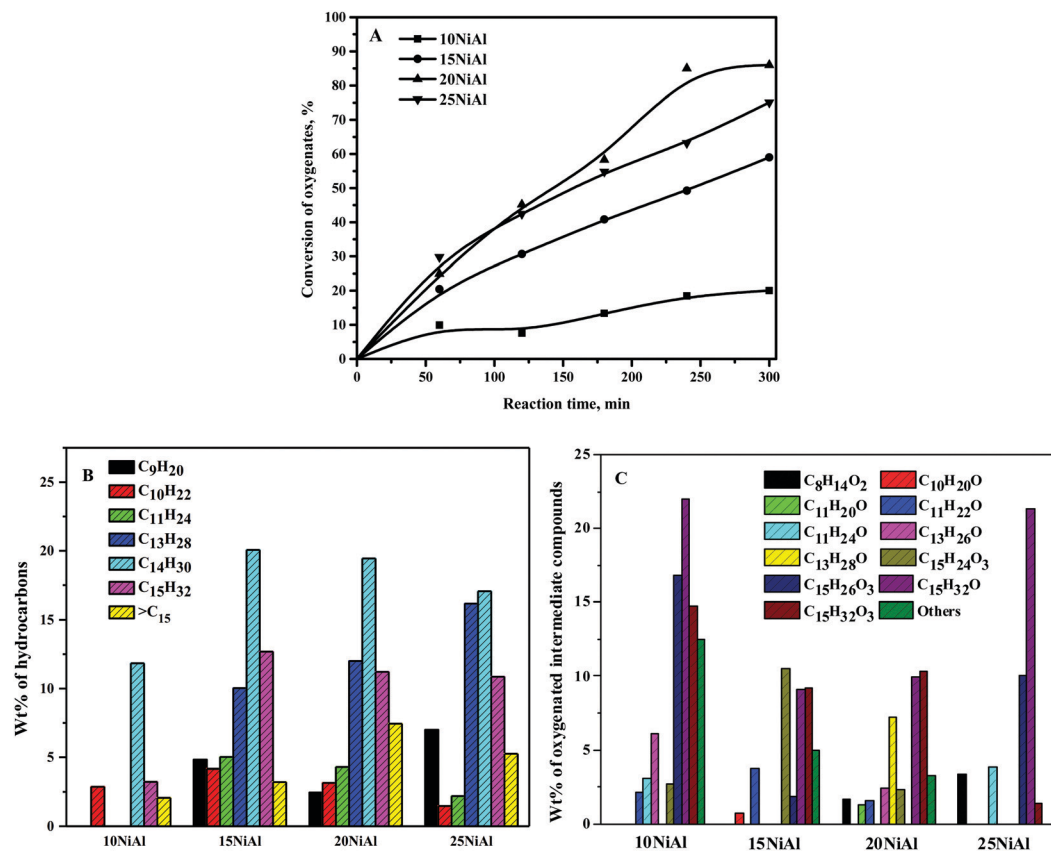


Fig. 7 Effect of nickel metal content on γ -Al₂O₃ on the (A) conversion of oxygenates and (B) wt% of hydrocarbons, and (C) wt% of oxygenated intermediate compounds. Reaction conditions: 0.5 g catalyst, 543 K, and 30 bar H₂. B and C: 20% conversion of oxygenates for 10NiAl and 60% conversion of oxygenates for 15NiAl, 20NiAl, and 25NiAl.

time, the conversion of oxygenates was around 17% at 523 K and reached around 85% at 543 K. However, almost complete conversion of oxygenates was achieved after 2 h of reaction time at 573 K. At 523 K, C₁₄ and C₁₅ alkanes were perceived as the primary hydrocarbons with only a small amount of lighter hydrocarbons (Fig. 8B). Besides, C₁₃ alkane was absent at 523 K. However, a significant quantity of the C₁₃ alkane was observed at 543 K and 573 K. At 573 K, C₁₃ alkane was, however, the dominating hydrocarbon. Furthermore, the wt% values of lighter hydrocarbons were quite significant at 543 K and 573 K. These results exhibited the enhancement of cracking reaction at elevated reaction temperatures.^{45,50} Moreover, only a trivial quantity of >C₁₅ alkanes was observed at 523 K. However, a significant quantity of >C₁₅ alkanes was observed at 543 K and 573 K. The condensation of oxygenated intermediate compounds (ketones) is favorable at elevated reaction temperatures with high wt% of >C₁₅ alkanes. At 523 K, the wt% of the furan ring hydrogenation product (C₁₅H₂₆O₃) was relatively higher compared to the furan ring opening products (C₁₅H₃₂O₃) (Fig. 8B). The furan ring hydrogenation product was, however, almost absent at 543 K and 573 K. On the contrary, a significant quantity of furan rings opening product was observed at 543 K and 573 K. This was due to the faster rate of ring hydrogenation and ring-opening reaction at elevated temperatures. At 573 K

and 2 h of reaction time, wt% values of alkanes at 100% conversion of oxygenates were as follows: 19.6% C₉H₂₀, 3.9% C₁₀H₂₂, 14.3% C₁₁H₂₄, 0.8% C₁₂H₂₆, 33.8% C₁₃H₂₈, 16.1% C₁₄H₃₀, 9.0% C₁₅H₃₂, and 2.5% >C₁₅. High wt% of C₁₃ alkane was due to the dominating cracking reaction at the high reaction temperature. At 543 K and 6 h of reaction time, the wt% values of alkanes at 85.8% conversion of oxygenates were as follows: 9.4% C₉H₂₀, 7.2% C₁₀H₂₂, 11.0% C₁₁H₂₄, 10.8% C₁₃H₂₈, 20.5% C₁₄H₃₀, 21.4% C₁₅H₃₂, and 5.4% >C₁₅.

3.7. Reproducibility and reusability of Ni/ γ -Al₂O₃

The reproducibility of experimental results for HDO of the C₁₅ fuel precursor was confirmed by conducting two reactions under similar reaction conditions over 20NiAl catalyst. The conversion of oxygenates and wt% of hydrocarbons and oxygenated intermediate compounds were almost identical for both runs (Table 2). At 300 min of reaction time, almost complete conversions of oxygenates (99.3% and 97.6%) with negligible wt% of oxygenated intermediate compounds were perceived for both the runs. In order to investigate the reusability of 20NiAl, the spent catalyst was filtered from both of these runs, and the adsorbed liquid was then removed by repeated ethanol wash. The separated catalyst was dried overnight in an oven at 373 K, followed by calcination at 823 K and activation by H₂ at 973 K.



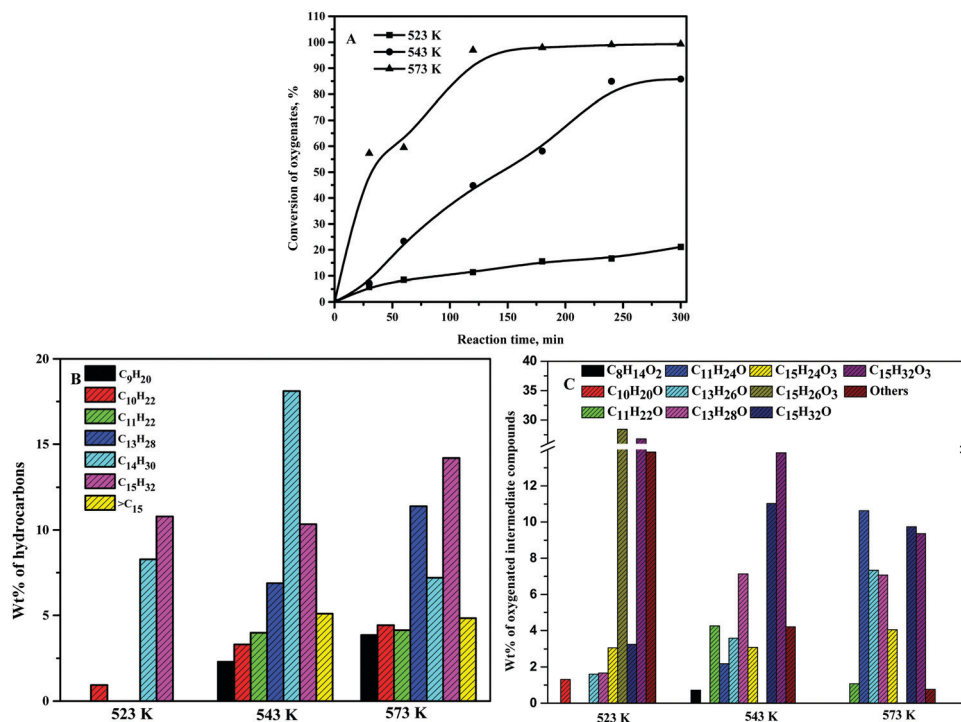


Fig. 8 Effect of reaction temperature on the (A) conversion of oxygenated compounds, (B) wt% of hydrocarbons, and (C) wt% of oxygenated intermediate compounds. Reaction conditions: 0.5 g 20NiAl and 30 bar H_2 . B and C: 20% conversion of oxygenates for 523 K and 50% conversion of oxygenates at other temperatures.

Table 2 Reproducibility and reusability of the 20NiAl catalyst

	Conversion of oxygenates at 300 min, %	Wt% of hydrocarbons at 60% conversion of oxygenates						
		C_9H_{20}	$C_{10}H_{22}$	$C_{11}H_{24}$	$C_{12}H_{26}$	$C_{13}H_{28}$	$C_{14}H_{30}$	$C_{15}H_{32}$
Run 1: fresh catalyst	99.3	5.8	2.1	3.4	6.7	20.6	15.6	5.8
Run 2: fresh catalyst	97.6	5.1	2.8	4.2	6.8	19.4	13.4	8.3
Run 3: regenerated catalyst	81.8	7.6	1.7	3.5	6.7	21.4	14.8	4.3

Reaction conditions: 0.5 g 20NiAl, 573 K, and 30 bar H_2 .

We performed a fresh HDO reaction using the regenerated catalyst under reaction conditions similar to that of the freshly prepared catalyst. The regenerated catalyst exhibited a somewhat lower conversion of oxygenates (82%) compared to that of the freshly prepared catalyst. The BET surface area of the regenerated catalyst ($142 \text{ m}^2 \text{ g}^{-1}$) was lower than that of the freshly prepared catalyst ($169 \text{ m}^2 \text{ g}^{-1}$) (Table 1). Furthermore, the metal dispersion of the regenerated catalyst was somewhat lesser with a slightly bigger nickel crystallite size compared to the freshly prepared catalyst. The HR-TEM image of the regenerated catalyst (54.8 nm) also exhibited a larger nickel particle size compared to that of the freshly prepared catalyst (27.8 nm) (Fig. S7, ESI[†]). Similarly, the regenerated catalyst exhibited slightly reduced acidity and lesser degree of reduction than those of the freshly prepared catalyst (Table 1 and Fig. S8, ESI[†]). The change in these catalyst characteristics was responsible for a slightly reduced catalytic activity of the regenerated catalyst than that of the freshly prepared catalyst.⁵⁰ However, the wt%

values of hydrocarbons for regenerated catalysts were comparable to those of the freshly prepared catalyst (Table 2).

4. Conclusions

The present study provides a systematic investigation of two-step conversion of furfural and 2-MF to jet fuel range (C_9 – C_{15} alkanes) hydrocarbon biofuel: (i) HAA reaction over the CER catalyst and (ii) HDO of the C_{15} fuel precursor over the Ni/ γ - Al_2O_3 catalyst. The optimum HAA reaction conditions were 1 g CER, 1:1 2-MF/furfural, and 328 K. The empirical kinetic model fairly corroborated the experimental HAA reaction data. The HAA reaction exhibited an activation energy of $15.09 \text{ kcal mol}^{-1}$. HDO of the C_{15} fuel precursor occurred through sequential furan ring hydrogenation and ring-opening reactions. The deoxygenation of furan ring-opening products then succeeded through a combination of



dehydroformylation and HDO reactions. The dehydroformylation reaction was the dominating pathway with C₁₄ alkane as the major hydrocarbon product. The HDO reaction was, however, enhanced at elevated hydrogen pressure with improved wt% of C₁₅ alkane. The catalytic activity was enhanced with rising Ni metal content on γ -Al₂O₃ without much effect on the wt% values of the products. The cracking reaction was substantial at elevated reaction temperatures with high wt% values of lighter hydrocarbons. Nearly complete conversion of oxygenates with 38.6 wt% < C₁₃, 33.8 wt% C₁₃, 16.1 wt% C₁₄, 9.0 wt% C₁₅, and 2.5 wt% > C₁₅ alkanes was observed over 20NiAl at 573 K and 2 h of reaction time.

Author contributions

Alekhya Kunamalla: Investigation and writing – original draft. Bhushan S. Shrirame: investigation. Sunil K. Maity: conceptualization, project administration, supervision, and writing – review and editing.

Nomenclatures

BET	Brunauer–Emmett–Teller
BJH	Barret–Joyner–Halenda
CER	Cation exchange resin
FID	Flame ionization detector
GC	Gas chromatography
HAA	Hydroxyalkylation–alkylation
HDO	Hydrodeoxygenation
2-MF	2-Methylfuran
MS	Mass spectrometry
NH ₃ -TPD	Temperature programmed desorption of ammonia
TEM	Transmission electron microscopy
TPR	Temperature programmed reduction
XRD	X-ray diffraction

Conflicts of interest

There is no conflict of interest.

Notes and references

- N. Jones, The outlook for energy: A view to 2040. https://www.connaissancedesenergies.org/sites/default/files/pdf-actualites/2016_outlook_for_energy_exxonmobil.pdf.
- M. N. A. M. Yusoff, N. W. M. Zulkifli, B. M. Masum and H. H. Masjuki, *RSC Adv.*, 2015, **5**, 100184–100211.
- S. K. Maity, *Renewable Sustainable Energy Rev.*, 2015, **43**, 1446–1466.
- P. Kumar, P. Kumar, P. V. C. Rao, N. V. Choudary and G. Sriganesh, *Fuel*, 2017, **199**, 339–345.
- D. C. Elliott, *Energy Fuels*, 2007, **21**, 1792–1815.
- F. Li, Y. Yuan, Z. Huang, B. Chen and F. Wang, *Appl. Catal., B*, 2015, **165**, 547–554.
- M. J. Tijmensen, A. P. Faaij, C. N. Hamelinck and M. R. van Hardeveld, *Biomass Bioenergy*, 2002, **23**, 129–152.
- S. K. Maity, *Renewable Sustainable Energy Rev.*, 2015, **43**, 1427–1445.
- K. Yan, G. Wu, T. Lafleur and C. Jarvis, *Renewable Sustainable Energy Rev.*, 2014, **38**, 663–676.
- A. S. May, S. M. Watt and E. J. Biddinger, *React. Chem. Eng.*, 2021, **6**, 2075–2086.
- G. W. Huber, J. N. Chheda, C. J. Barrett and J. A. Dumesic, *Science*, 2005, **308**, 1446–1450.
- R. M. West, Z. Y. Liu, M. Peter and J. A. Dumesic, *ChemSusChem*, 2008, **1**, 417–424.
- A. Corma, O. de la Torre and M. Renz, *ChemSusChem*, 2011, **4**, 1574–1577.
- G. Li, N. Li, Z. Wang, C. Li, A. Wang, X. Wang, Y. Cong and T. Zhang, *ChemSusChem*, 2012, **5**, 1958–1966.
- T. Wang, K. Li, Q. Liu, Q. Zhang, S. Qiu, J. Long, L. Chen, L. Ma and Q. Zhang, *Appl. Energy*, 2014, **136**, 775–780.
- A. Corma, O. de la Torre, M. Renz and N. Villandier, *Angew. Chemie*, 2011, **123**, 2423–2426.
- G. Li, N. Li, J. Yang, A. Wang, X. Wang, Y. Cong and T. Zhang, *Bioresour. Technol.*, 2013, **134**, 66–72.
- W. Wang, N. Li, S. Li, G. Li, F. Chen, X. Sheng, A. Wang, X. Wang, Y. Cong and T. Zhang, *Green Chem.*, 2016, **18**, 1218–1223.
- S. Li, N. Li, G. Li, L. Li, A. Wang, Y. Cong, X. Wang, G. Xu and T. Zhang, *Appl. Catal., B*, 2015, **170**, 124–134.
- C. Zhu, T. Shen, D. Liu, J. Wu, Y. Chen, L. Wang, K. Guo, H. Ying and P. Ouyang, *Green Chem.*, 2016, **18**, 2165–2174.
- G. Li, N. Li, S. Li, A. Wang, Y. Cong, X. Wang and T. Zhang, *Chem. Commun.*, 2013, **49**, 5727–5729.
- S. Li, N. Li, W. Wang, L. Li, A. Wang, X. Wang and T. Zhang, *Sci. Rep.*, 2016, **6**, 4–10.
- I. Yati, M. Yeom, J. W. Choi, H. Choo, D. J. Suh and J. M. Ha, *Appl. Catal., A*, 2015, **495**, 200–205.
- Q. Deng, P. Han, J. Xu, J.-J. Zou, L. Wang and X. Zhang, *Chem. Eng. Sci.*, 2015, **138**, 239–243.
- S. Li, N. Li, G. Li, L. Li, A. Wang, Y. Cong, X. Wang and T. Zhang, *Green Chem.*, 2015, **17**, 3644–3652.
- X. Zhang, Q. Deng, P. Han, J. Xu, L. Pan, L. Wang and J.-J. Zou, *AIChE J.*, 2017, **63**, 680–688.
- D. Damodar, A. Kunamalla, M. Varkolu, S. K. Maity and A. S. Deshpande, *ACS Sustainable Chem. Eng.*, 2019, **7**, 12707–12717.
- S. Liu, T. R. Josephson, A. Athaley, Q. P. Chen, A. Norton, M. Ierapetritou, J. I. Siepmann, B. Saha and D. G. Vlachos, *Sci. Adv.*, 2019, **5**, 1–9.
- C. Wen, E. Barrow, J. Hattrick-Simpers and J. Lauterbach, *Phys. Chem. Chem. Phys.*, 2014, **16**, 3047–3054.
- K. Li, F. Zhou, X. Liu, H. Ma, J. Deng, G. Xu and Y. Zhang, *Catal. Sci. Technol.*, 2020, **10**, 1151–1160.
- A. Samikannu, L. J. Konwar, K. Rajendran, C. C. Lee, A. Shchukarev, P. Virtanen and J. P. Mikkola, *Appl. Catal., B*, 2020, **272**, 118987.
- D.-H. Liu, H.-L. He, J.-J. Wang, S.-Y. Zhou, T. Zeng, X.-Y. Gao, Y. Xiao, X. Yi, A. Zheng, Y.-B. Zhang and Z. Li, *Green Chem.*, 2021, **23**, 9974–9981.



- 33 H. Li, Z. Gui, S. Yang, Z. Qi, S. Saravanamurugan and A. Riisager, *Energy Technol.*, 2018, **6**, 1060–1066.
- 34 S. R. Yenumala, S. K. Maity and D. Shee, *Catal. Sci. Technol.*, 2016, **6**, 3156–3165.
- 35 P. Kumar, S. R. Yenumala, S. K. Maity and D. Shee, *Appl. Catal., A*, 2014, **471**, 28–38.
- 36 R. Kumar, K. Kumar, N. V. Choudary and K. K. Pant, *Fuel Process. Technol.*, 2019, **186**, 40–52.
- 37 S. Liu, S. Dutta, W. Zheng, N. S. Gould, Z. Cheng, B. Xu, B. Saha and D. G. Vlachos, *ChemSusChem*, 2017, **10**, 3225–3234.
- 38 S. Dutta and B. Saha, *ACS Catal.*, 2017, **7**, 5491–5499.
- 39 E. Furimsky, *Appl. Catal., A*, 1983, **6**, 159–164.
- 40 E. Furimsky, *Appl. Catal., A*, 2000, **199**, 147–190.
- 41 S. Liu, W. Zheng, J. Fu, K. Alexopoulos, B. Saha and D. G. Vlachos, *ACS Catal.*, 2019, **9**, 7679–7689.
- 42 V. C. S. Palla, D. Shee and S. K. Maity, *RSC Adv.*, 2014, **4**, 41612–41621.
- 43 X. Yang, R. W. Jenkins, J. H. Leal, C. M. Moore, E. J. Judge, T. A. Semelsberger and A. D. Sutton, *ACS Sustainable Chem. Eng.*, 2019, **7**, 14521–14530.
- 44 B. Hočevar, M. Grilc, M. Huš and B. Likozar, *Appl. Catal., B*, 2017, **218**, 147–162.
- 45 G. Li, N. Li, J. Yang, L. Li, A. Wang, X. Wang, Y. Cong and T. Zhang, *Green Chem.*, 2014, **16**, 594–599.
- 46 S. Li, N. Li, G. Li, A. Wang, Y. Cong, X. Wang and T. Zhang, *Catal. Today*, 2014, **234**, 91–99.
- 47 E. I. Gürbüz, E. L. Kunkes and J. A. Dumesic, *Appl. Catal., B*, 2010, **94**, 134–141.
- 48 T. Morioka, A. Nishizawa, T. Furukawa, M. Tobisu and N. Chatani, *J. Am. Chem. Soc.*, 2017, **139**, 1416–1419.
- 49 J. Yang, N. Li, S. Li, W. Wang, L. Li, A. Wang, X. Wang, Y. Cong and T. Zhang, *Green Chem.*, 2014, **16**, 4879–4884.
- 50 Q. Xia, Y. Xia, J. Xi, X. Liu, Y. Zhang, Y. Guo and Y. Wang, *ChemSusChem*, 2016, **10**, 747–753.

